

Dilution of boundary layer cloud condensation nucleus concentrations by free tropospheric entrainment during marine cold air outbreaks

F. Tornow^{1,2}, A. S. Ackerman², A. M. Fridlind², B. Cairns², E. C. Crosbie^{3,4}, S. Kirschler^{5,6}, R. H. Moore³, C. E. Robinson^{3,4}, C. Seethala⁷, M. A. Shook³, C. Voigt^{5,6}, E. L. Winstead^{3,4}, L. D. Ziembra³, P. Zuidema⁷, A. Sorooshian^{8,9}

¹Earth Institute, Columbia University, NY, 10025, NY
²NASA Goddard Institute for Space Studies, NY, 10025, NY

²NASA Goddard Institute for Space Studies, NY, 10025, NY
³NASA Langley Research Center, Hampton, VA 23681, USA

³NASA Langley Research Center, Hampton, VA 23681, USA
Science Systems and Applications, Inc., Hampton, VA 23681, USA

⁴Science, Systems, and Applications, Inc., Hampton, VA 23681, USA
 sches Zentrum für Luft- und Raumfahrt (DLR), Oberpfaffenhofen, Germany

⁶ Johannes Gutenberg-Universität, Mainz, Germany

Marine and Atmosphere Science, University of Miami

⁸Department of Chemical and Environmental Engineering, University of Arizona, Tucson, Arizona, 85721-8877, USA

Department of Chemical and Environmental Engineering, University of Arizona, Tucson, Arizona, 85721,
USA

⁹Department of Hydrology and Atmospheric Sciences, University of Arizona, Tucson, Arizona, 85721, USA

Sciences

Key Points:

- Recent aircraft measurements enable an analysis of cloud condensation nuclei (CCN) during marine cold air outbreaks.
 - CCN concentrations are usually less in the free troposphere than in the marine boundary layer over the northwest Atlantic.
 - A boundary layer CCN budget indicates a leading role of entrainment dilution upwind of cloud regime transition.

25 **Abstract**

26 Recent aircraft measurements over the northwest Atlantic enable an investigation of how
 27 entrainment from the free troposphere (FT) impacts cloud condensation nuclei (CCN)
 28 in the marine boundary layer (MBL) during cold-air outbreaks (CAOs), motivated by
 29 the role of CCN in mediating transitions from closed to open-cell regimes. Observations
 30 compiled over eight flights indicate predominantly far lesser CCN concentrations in the
 31 FT than in the MBL. For one flight, a fetch-dependent MBL-mean CCN budget is com-
 32 piled from estimates of sea-surface fluxes, entrainment of FT air, and hydrometeor collision-
 33 coalescence, based on in-situ and remote-sensing measurements. Results indicate a dom-
 34 inant role of FT entrainment in reducing MBL CCN concentrations, consistent with satellite-
 35 observed trends in droplet number concentration upwind of CAO cloud-regime transi-
 36 tions over the northwest Atlantic. Relatively scant CCN may widely be associated with
 37 FT dry intrusions, and should accelerate cloud regime transitions where underlying MBL
 38 air is CCN-rich, thereby reducing regional albedo.

39 **Plain Language Summary**

40 Cloud droplets form on a subset of atmospheric particles, referred to as cloud con-
 41 densation nuclei (CCN). The number concentration of CCN affects the brightness and
 42 horizontal extent of clouds. We use aircraft measurements from several flights where cold
 43 continental air flowing over the northwest Atlantic generates swiftly evolving clouds in
 44 the near-surface turbulent air, referred to as the marine boundary layer (MBL). We show
 45 that CCN concentrations in the immediately overlying air, the free troposphere (FT),
 46 are usually far less than in the MBL. Through additional analysis of one flight, we show
 47 that mixing of FT air is the primary factor reducing CCN concentrations in the MBL
 48 prior to rain formation.

49 **1 Introduction**

50 Extratropical marine boundary layer (MBL) clouds typically occupy the postfrontal
 51 sector of synoptic systems when passing over the ocean surface (e.g., Field & Wood, 2007;
 52 Rémillard & Tselioudis, 2015). Their presence substantially enhances regional albedo,
 53 and such clouds are challenging to faithfully represent in numerical models, whether for
 54 forecasting weather or projecting climate change (e.g., Bodus-Salcedo et al., 2016; Forbes
 55 & Ahlgrimm, 2014; Tselioudis et al., 2021). Common during winter and its shoulder sea-
 56 sons, cold air outbreaks (CAOs) pose a particular challenge (e.g., Abel et al., 2017; Field
 57 et al., 2017) as they form highly reflective, nearly overcast cloud decks, typically orga-
 58 nized in roll-like structures that contain both water and ice, which generally break up
 59 into less reflective, open-cellular cloud fields farther downwind (e.g., Brümmer, 1999; Pi-
 60 than et al., 2019).

61 MBL clouds are sensitive to the number concentration of aerosol available as cloud
 62 condensation nuclei (CCN). Greater CCN concentrations can enhance cloud albedo when
 63 (1) distributing the same cloud condensate over more numerous, smaller droplets (Twomey,
 64 1974), (2) suppressing precipitation formation, leading to greater areal cloud cover (Albrecht,
 65 1989) and thicker clouds (Pincus & Baker, 1994), and (3) affecting cloud mesoscale struc-
 66 ture (e.g., H. Wang & Feingold, 2009). On the other hand, smaller droplets fall more slowly
 67 in updrafts and can boost entrainment of overlying dry air, reducing cloud thickness and
 68 counteracting albedo-enhancing effects (Ackerman et al., 2004; Bretherton et al., 2007).
 69 The collisions between hydrometeors that drive precipitation formation in warm clouds
 70 also reduce CCN number concentrations and can drive a positive feedback loop in which
 71 fewer CCN promote further precipitation formation in warm stratocumulus (Yamaguchi
 72 et al., 2017). Such a feedback loop is also implicated in mixed-phase CAO observations
 73 (e.g., Abel et al., 2017) and simulations (Tornow et al., 2021), and is hypothesized to ex-

74 plain horizontal gradients in cloud droplet number concentrations off the mid-Atlantic
 75 coast of the US (Dadashazar et al., 2021).

76 Unique to CAOs are extreme surface heat fluxes that typically drive rapid MBL
 77 deepening despite strong large-scale subsidence (Papritz et al., 2015; Papritz & Spen-
 78 gler, 2017), thereby copiously entraining free tropospheric (FT) air. Entrained FT air
 79 in turn can strongly affect MBL air, where each has been variously influenced by a wide
 80 variety of sinks and sources, including new particle formation (e.g., I. L. McCoy et al.,
 81 2021; Zheng et al., 2021) and long-range transport of direct emissions, such as biomass
 82 burning (e.g., Zheng et al., 2020).

83 In previous work, simulated MBL clouds in a northwest Atlantic CAO case study
 84 were found sensitive to idealized FT–MBL differences in CCN concentration (Tornow
 85 et al., 2021). The present study seeks to establish observationally the degree to which
 86 the FT serves as a CCN sink or source to the evolving cloudy MBL in CAOs in that re-
 87 gion. This wider analysis is enabled by recent in-situ and remote-sensing observations
 88 collected on multiple research flights during the Aerosol Cloud Meteorology Interactions
 over the Western Atlantic Experiment (ACTIVATE; Sorooshian et al., 2019).

90 2 Material and Methods

91 We analyze all CAO research flights conducted during ACTIVATE in 2020 (Ta-
 92 ble S1). For assessment of the CCN budget, we use the second research flight on 1 March
 93 2020 (RF14), which reached farthest downwind into the offshore cloud deck, nearly reach-
 94 ing the transition from overcast to broken states. For each of the eight CAO research
 95 flights in 2020, we use in-situ and remote-sensing measurements (Table S2), collected via
 96 Falcon and King Air aircraft, respectively. We collocate all in-situ data by their time stamp
 97 and associated remote-sensing products nearest in geolocation to the Falcon aircraft at
 98 a given time. Figure 1 provides a composite overview of collocated data from RF14.

99 The following subsections describe the CCN observations (Section 2.1), process-
 100 ing of data from multiple research flights (Section 2.2), and the MBL CCN budget anal-
 101 ysis for RF14 (Section 2.3).

102 2.1 In-situ aerosol measurements

103 A Droplet Measurement Technologies (DMT) CCN counter (Roberts & Nenes, 2005;
 104 Lance et al., 2006) was operated in one of two modes:

- 105 (1) constant supersaturation (SS; usually set to 0.43%) or
- 106 (2) SS scanning (typically covering 0.2–0.7%; Moore & Nenes, 2009)

107 To compare data from all eight research flights (Section 3), we interpolate CCN from mode
 108 (2) operations to SS = 0.43% per leg using polynomial regression (described further be-
 109 low). We also use condensation nuclei (CN) counts of particles with diameters greater
 110 equal 10 nm via the TSI Condensation Particle Counters 3772 instrument.

111 2.2 Processing of ACTIVATE measurements

112 2.2.1 Classification of *in-situ* legs

113 Samples acquired at 1 Hz frequency are separated into flight legs, where each leg
 114 is defined as a consecutive period of CCN measurements uninterrupted by missing val-
 115 ues (usually spanning ~50 s periods). This separation triples the number of legs com-
 116 pared to using horizontal segments (cf. Sorooshian et al., 2019) and requires a refined
 117 leg type classification:

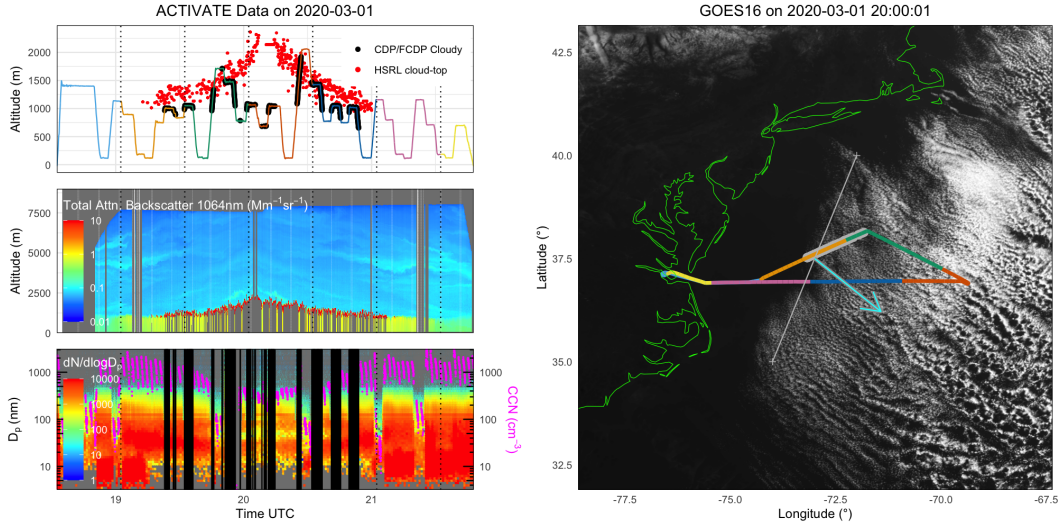


Figure 1. ACTIVATE Falcon flight track during RF14 (top left and right), King-Air remote-sensing measurements (top and middle left), Falcon in-situ measurements of aerosol PSD and CCN concentrations (bottom left), and GOES-16 image (right) with approximate wind direction inferred from roll orientation (cyan line), cloud edge (white line), and RSP measurement extent (thick gray below track).

- 118 (1) Using liquid water contents (LWCs) measured by the Fast Cloud Droplet Probe
 119 (FCDP; for particle diameters 3-50 um) and the Two-Dimensional Stereo (2DS)
 120 probe (Lawson et al., 2006, particle diameters 51-1465 um), we define cloudy sam-
 121 ples as those with $LWC_{FCDP} + LWC_{2DS} \geq 0.05 \text{ g m}^{-3}$ and classify legs with at
 122 least 5 such samples as “cloudy”.
 123 (2) To classify the remaining clear legs by their relative altitude to nearby clouds, we
 124 collect the cloudy samples near each leg (within 15 min of mean leg time or within
 125 45 min if 15 min provides fewer than 5 cloudy samples) and define the local cloud-
 126 base and cloud-top heights (CBH, CTH) from maximum and minimum altitudes,
 127 respectively, of the nearest cloudy samples (the closest 15% in time from mean leg
 128 time among samples collected) to crudely account for the spatial heterogeneity of
 129 clouds (e.g., the swiftly evolving CTH seen in Figure 1).
 130 (3) Finally, we label each cloud-free leg by comparing its maximum and minimum al-
 131 titudes (H_{\max}, H_{\min}) to CTH and CBH +/- a 50 m buffer to better separate FT
 132 from MBL legs and to avoid the entrainment interfacial layer (e.g., Dadashazar
 133 et al., 2018):
 134 “clear, below-cloud”: $H_{\max} < (CBH - 50 \text{ m})$
 “clear, above-cloud”: $H_{\min} > (CTH + 50 \text{ m})$ or if
 $H_{\min} > (CBH - 50 \text{ m})$ and $H_{\max} > (CTH + 50 \text{ m})$
 relevant for legs during ascents and descents
 “clear, cloud-level”: all remaining samples above or at 500 m
 “clear, near-surface”: all remaining samples below 500 m

135 Figure S1 shows the resulting classification for RF14, with 90 legs identified.

136 2.2.2 Projection into quasi-Lagrangian framework

137 In an ideal scenario for our analysis, all measurements would be available in a mov-
 138 ing Lagrangian column of MBL air as it moves downwind. Lacking such a scenario, we

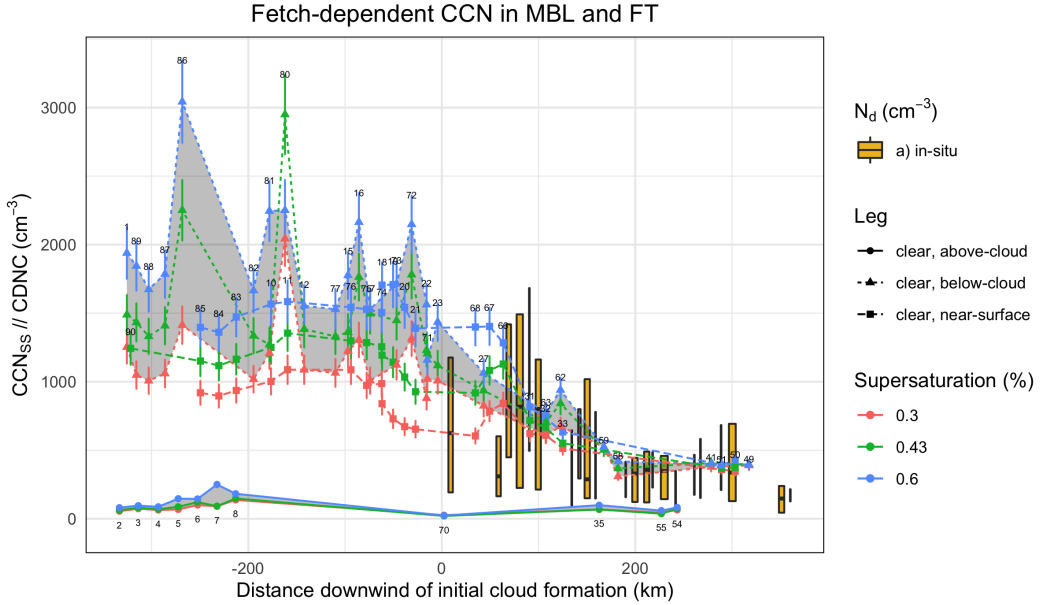


Figure 2. CCN at selected supersaturations (by color) versus ΔL derived from cloud-free samples on RF14. Leg types distinguished per legend. Gray shading spans FT class “clear, above-cloud” and MBL class “clear, below-cloud”. Orange bars span middle half of in-cloud N_d from FCDP, with median indicated.

roughly emulate a Lagrangian framework by projecting all measurements onto a wind field and using horizontal distance from the upwind cloud edge, ΔL , as a transformed coordinate system.

From geostationary imagery we approximate a field-wide MBL wind direction from the roll orientation, assuming zero angular offset, and draw a great circle to mark the initial cloud edge (Figure 1). We then use each leg’s geolocation and the wind direction to determine the intercept point on the cloud edge up- or downwind of the leg coordinates and measure the geodetic distance between leg coordinates and this intercept point.

Figure 2 illustrates the resulting range $\Delta L \in [\pm 300 \text{ km}]$ for RF14 corresponding to the Figure 1 scene. We note that MBL wind direction and roll orientation can be offset by up to $\pm 20\text{--}30^\circ$ (Etling & Brown, 1993; Atkinson & Wu Zhang, 1996), corresponding to a range error of about $\pm 10 \text{ km}$ per 100 km.

2.3 MBL CCN budget

2.3.1 Entrainment

To estimate the entrainment rate (w_e) of FT air at the top of the MBL we use CO trace gas measurements (Figure S2) and rely on a simple mixed-layer approach (e.g., Lilly, 1968; Fridlind et al., 2012) to characterize the evolution of the MBL-mean mixing ratio of species X (here applied to CO to estimate the entrainment rate, and later used for the budget of $\text{CCN}_{\text{SS}=0.43\%}$). Note that we apply this approach to a horizontally translating quasi-Lagrangian domain and use MBL-averaged quantities (denoted with overbar), invoking the Lagrangian derivative:

$$\frac{d\bar{X}}{dt} = S_{\text{int}} + S_{\text{surf}} + S_{\text{entr}} \quad (1)$$

161 with net sources from internal processes, surface fluxes, and FT entrainment at the MBL
 162 top (inversion base height z_i), where

$$163 \quad S_{\text{entr}} = \frac{\Delta \bar{X}}{z_i} w_e \quad (2)$$

164 given the jump at the top of the MBL $\Delta \bar{X} = X_{\text{FT}} - \bar{X}$ and entrainment rate $w_e =$
 165 $\frac{dz_i}{dt} - w_{\text{LS}}$, with large-scale vertical wind w_{LS} . Internal process and surface sources are
 166 assumed zero for CO.

167 After combining Equations 1 and 2, we solve for w_e using the horizontal gradient
 168 in distance downwind s to evaluate the Lagrangian derivative:

$$169 \quad \frac{d\bar{X}}{dt} = \frac{d\bar{X}}{ds} \frac{ds}{dt} = \frac{\bar{X}(\Delta L + 50\text{km}) - \bar{X}(\Delta L - 50\text{km})}{250\text{km}} u \quad (3)$$

170 with horizontal wind speed u taken at 500 m from an ERA5 profile on 1 March 2020 20:00
 171 UTC, at 36.90°N, 69.35°W.

172 In these equations \bar{X} , X_{FT} , and z_i are computed from separate 4th-order polynomial
 173 fits versus ΔL . For fitting \bar{X} , we use “clear, near-surface” and “clear, below-cloud”,
 174 whereas for X_{FT} we use “clear, above-cloud”. For CO measurements as X_{FT} we linearly
 175 fit in-situ data (Figure S2) and for z_i we linearly fit HSRL-2 CTH (Figure S3).

176 Once w_e is estimated, we compute S_{entr} from Equation 2 using fits to the CCN data
 177 (Figure 2).

178 2.3.2 Hydrometeor collisions

179 We use in-situ FCDP and 2DS measurements to estimate collision-coalescence rates.
 180 We first parse the data into 5-s intervals (~ 500 m horizontal distances). Per interval, we
 181 bin-wise average droplet size distributions from both instruments. We then compute collision-
 182 coalescence loss rates by integrating the simplified stochastic collection equation (cf. Wood,
 183 2006):

$$184 \quad \dot{N}_{\text{coll}} = -\frac{1}{2} \int_0^\infty \int_0^\infty n(x) K(x', x) n(x') dx dx' \quad (4)$$

185 in which $K(x, x')$ is the collection kernel from Hall (1980) across radius bins x and x'
 186 (assuming a coalescence efficiency of unity for simplicity):

$$187 \quad K(x, x') = \pi[r(x) + r(x')]^2 E_{\text{coll}} |v(x) - v(x')| \quad (5)$$

188 where $n(x)$ is the measured hydrometeor number concentration, $r(x)$ the volume-mean
 189 radius for each bin, and droplet fall speed v is computed following Böhm (1992). Figure S4 shows two examples, demonstrating the impact of larger hydrometeors, as well
 190 as the estimated contribution to \dot{N}_{coll} from riming computed by summing over bins with
 191 frozen hydrometeors using the same kernel.

192 To obtain MBL-effective collision-coalescence rates some assumptions must be made
 193 about the vertical structure of clouds within the MBL. We guide these assumptions us-
 194 ing HSRL-2-based CTH and RSP-retrieved liquid water path (LWP) values projected
 195 onto the semi-Lagrangian framework (Section 2.2) to derive synthetic cloud profiles with
 196 stochastically drawn in-situ intervals that satisfy some proximity criteria.

197 We begin with RSP LWP retrievals. Discretizing the atmosphere into 50-m thick
 198 layers, we start at the layer closest to cloud top (from median of HSRL-2 CTH values
 199 within 100 s of an RSP measurement) and consider in-situ data for stochastic sampling
 200 obtained vertically within 50 m of the layer, within 100 km horizontally of the RSP ob-
 201 servation, and within 15 min of RSP acquisition. If these criteria produce no samples,
 202 we drop spatial and temporal proximity thresholds and, if still short on samples, relax
 203 the vertical constraint. Once a layer is assigned a sample (LWC, cloud droplet number
 204 concentration N_d , and \dot{N}_{coll}), we proceed downward until the vertical LWC integral matches
 205 the RSP LWP, but not past cloud base (the lowest layer in which clouds were observed

in-situ, ~ 700 m for RF14). For large LWP values ($>300 \text{ g m}^{-2}$), the cloud thickness is insufficient and though the reconstructed LWPs fall short, they are retained (Figure S3 inset). Figure S3 also shows profiles along ΔL and Figure S5 shows profile details. To match other budget terms we compute a 100-km running mean excluding cloud-free gaps.

Unfortunately, RSP only provides LWP values where the sun-observer geometry is favorable. For the case shown in Figure 1, these correspond to the northwest-most leg, shaded gray in Figure 4. As described further below, we use Moderate Resolution Imaging Spectroradiometer (MODIS) LWP retrievals to extend the analysis downwind.

2.3.3 Uncertainty

To estimate uncertainties, we apply Gaussian error propagation. Individual uncertainties associated with \bar{X} , X_{FT} , and z_i are taken from each fit's 95% confidence interval. These errors dominate when used in differentials, such as equation 3 (e.g., for \dot{N}_{tot} shown as dark blue bar in Figure 4). We assume 10-km uncertainty for ΔL , as already described. Assumed errors for ERA-5 variables are 10% (Seethala et al., 2021; Li et al., 2021). The error for \dot{N}_{coll} is estimated as the standard deviation across the locally available population, chosen because substantial sample variability (Figure S5) likely exceeds conventional error propagation.

3 Results

3.1 FT-MBL CCN gap

Figure 2 illustrates the processed CCN measurements for RF14, demonstrating the analysis approach applied to all flights. The differences between “clear, near-surface” and “clear, below-cloud” samples are smaller than the variability within each group, consistent with relatively well-mixed conditions within a turbulent MBL. Upwind of the cloud edge, entrainment of FT air can only reduce the MBL CCN, since the FT concentrations (at SS = 0.3-0.6%) are relatively stable at $50\text{-}200 \text{ cm}^{-3}$, much less than MBL concentrations of $1000\text{-}3000 \text{ cm}^{-3}$. Furthermore, the CCN gap between FT and MBL progressively narrows downwind of the cloud edge ($\Delta L > 0 \text{ km}$) from decreasing MBL concentrations, consistent with dilution via strong FT entrainment (quantified below). At all downwind distances sampled during this flight, FT concentrations are well exceeded by those in the MBL.

Another prominent feature in Figure 2 is the CCN spectral width decreasing downwind of cloud formation: upwind ($\Delta L \approx -300 \text{ km}$) nearly double the particles are available for activation as SS increases from 0.3 to 0.6%, whereas downwind ($\Delta L \approx 200 \text{ km}$) only $\sim 20\%$ more particles are available when doubling SS, a trend likely resulting from collisions between hydrometeors affecting aerosol PSD, specifically over diameters 50–80 nm (Figure S6), and composition (Figure S7).

To assess whether the FT commonly dilutes MBL CCN in northwest Atlantic CAOs, in Figure 3a we plot MBL versus FT $\text{CCN}_{\text{SS}=0.43\%}$ (hereafter just “CCN”) concentrations matched by ΔL . Overall, FT concentrations are predominantly exceeded by those in the MBL with rare exceptions. Some instances (e.g., “RF17 20200308-L1”) may be associated with variability of upwind MBL CCN (Figure S8), discussed further in Section 4. Because supersaturations in CAO convection can be expected to exceed 0.43%, we also evaluate how particles activating at greater supersaturations affect the FT-MBL differences. We repeat our analysis using the measurement of condensation nuclei (CN) larger than 10 nm (Figure 3b), which include sizes far smaller than are likely activated in MBL clouds, and find qualitatively similar gaps.

Figure 3a also shows that the FT-MBL CCN gap generally narrows downwind of cloud formation because of decreasing MBL concentrations (open symbols tend to lie to the left of closed symbols), consistent with RF14 (Figure 2). Meanwhile, FT concentra-

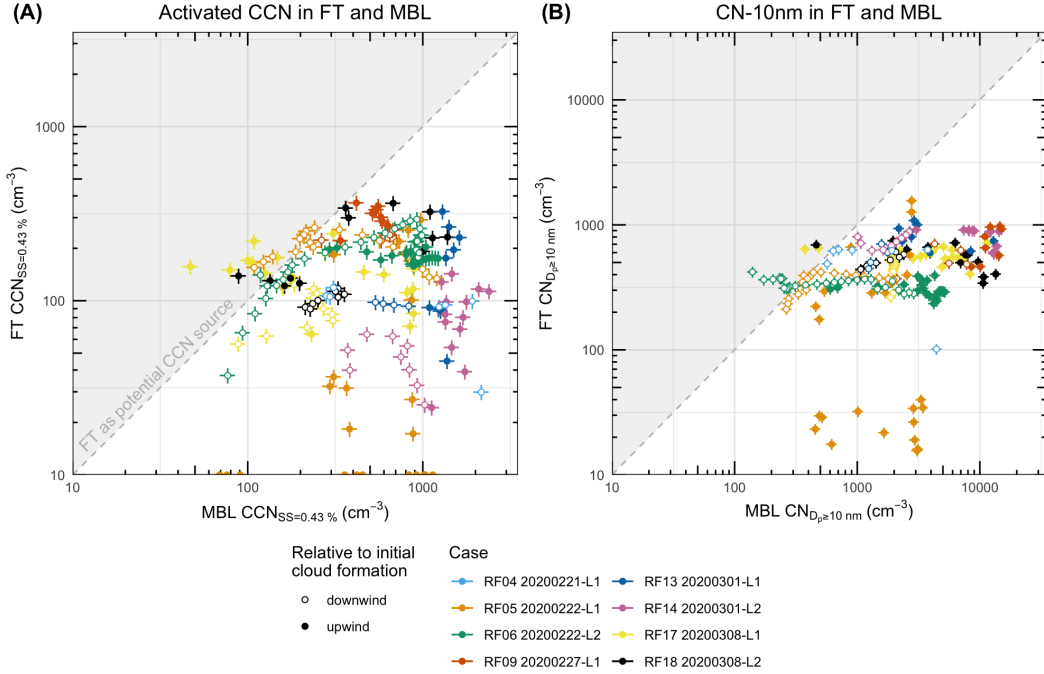


Figure 3. FT versus MBL concentration of CCN at 0.43% supersaturation (left) and of CN greater than 10 nm diameter (right) colored by research flight (per legend) and interpolated at 25-km intervals across available ΔL .

tions generally lack systematic trends with downwind distance and are characterized by a much smaller absolute dynamic range (cf. Figure 2).

3.2 Processes affecting FT–MBL gap

For RF14, we further estimate the relative contribution of FT entrainment to MBL CCN evolution. As described in Section 2, FT entrainment is approximated using CO measurements in the MBL and FT (Figure S2), yielding a rate of up to 12 cm s^{-1} for $0 < \Delta L < 100 \text{ km}$ (Figure S2 inset). This entrainment rate is applied to the CCN MBL–FT difference to estimate a CCN entrainment source. We also estimate a MBL-mean collision-coalescence CCN loss rate as described in Section 2 and a sea-salt surface source following Wood et al. (2017), as originally formulated by Clarke et al. (2006): $\dot{N}_{\text{surf}} = \frac{F u_s^{3.41}}{z_i}$, where $F = 132 \text{ m}^{-3} (\text{m s}^{-1})^{-2.41}$ and near-surface wind speed u_s is taken from the ERA5 profile. This budget framework is first applied to available RSP retrievals, which for this flight are at $0 < \Delta L < 100 \text{ km}$, well upwind of the cloud transition (Figure 1).

Results in Figure 4 indicate that the observed evolution in MBL CCN concentration ($\sim -240 \text{ cm}^{-3} \text{ h}^{-1}$) is primarily explained by FT entrainment ($\sim -180 \text{ cm}^{-3} \text{ h}^{-1}$), while hydrometeor collisions are less important ($\sim -25 \text{ cm}^{-3} \text{ h}^{-1}$) and surface production is quite modest ($\sim 5 \text{ cm}^{-3} \text{ h}^{-1}$). These relative contributions to the CCN budget are consistent with the aforementioned northwest Atlantic CAO simulations that used idealized aerosol in the absence of in situ measurements (cf. Figure 6 of Tornow et al., 2021). MODIS LWPs (acquired at 1730 UTC, 1 h before the flight) allow the budget to be extended downwind (dashed lines in Figure 4) and reveal a growing role for hydrometeor collisions approaching the cloud transition, from larger drops as well as frozen hydrometeors (riming).

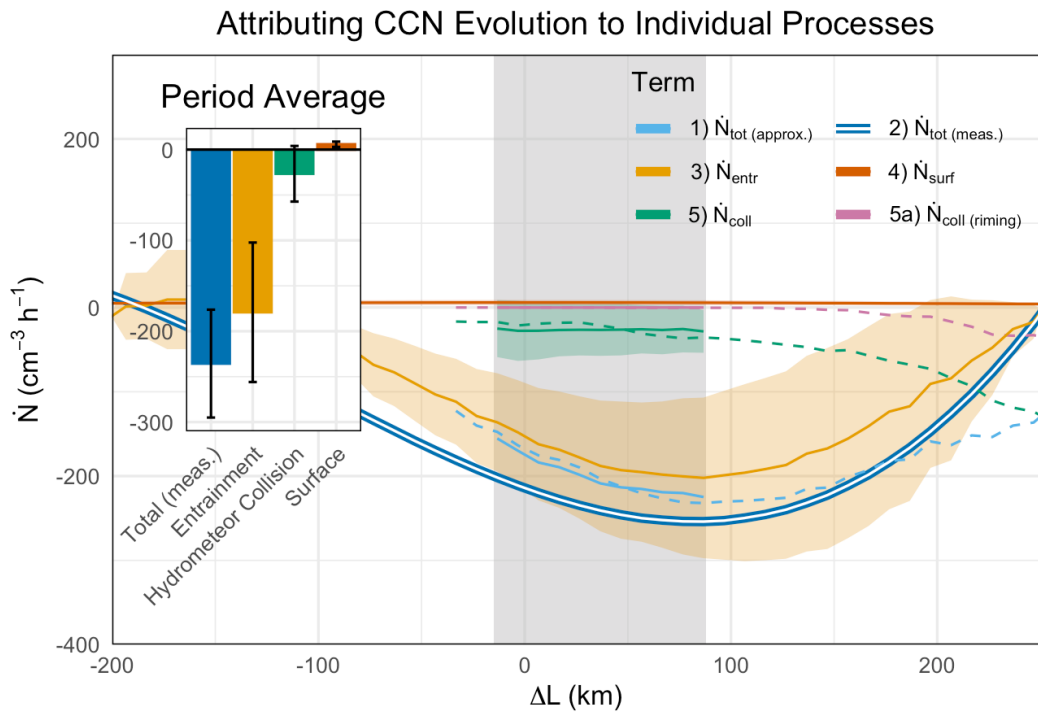


Figure 4. Quasi-Lagrangian MBL CCN budget terms versus ΔL for RF14: FT entrainment (orange), hydrometeor collisions (green) and contribution of riming (pink), surface source (red), their sum (light blue), and measured change of $\text{CCN}_{\text{ss}}=0.43\%$ (dark blue with white stripe). Rates using MODIS LWP retrievals (dashed lines) extend those from RSP (shaded area). Inset: mean values over shaded area with uncertainties (+/- one standard error).

279 **4 Discussion**

280 FT entrainment appears to be a plausible leading explanation for satellite-observed
 281 N_d gradients close to the US East Coast during winter (Painemal et al., 2021). Such N_d
 282 gradients are particularly strong during CAOs (Dadashazar et al., 2021), coincident with
 283 rapidly rising cloud tops despite strong large-scale subsidence (together implying great
 284 entrainment rates), and upwind of intense precipitation, where collisional loss rates are
 285 greater. Dadashazar et al. (2021) furthermore suggest a similar FT–MBL CCN differ-
 286 ence from aerosol extinction retrievals. Our findings are also consistent with CAO sim-
 287 ulations (Tornow et al., 2021), which yield comparable entrainment rates (Figure S2 in-
 288 set) and relative roles of FT entrainment and hydrometeor collisional loss upwind of in-
 289 tense precipitation.

290 An obvious question arises: where did such relatively clean FT air originate? Back-
 291 trajectories arriving at 2 and 3 km for RF14 (Figure S9) indicate a northwest origin, re-
 292 spectively starting seven days earlier near Alaska and the north Pacific and reaching \sim 6
 293 km before subsiding. Mass spectrometry data (Figure S7) indicate an FT aerosol com-
 294 posed mainly of sulfate whereas MBL aerosol varies more in composition with either sul-
 295 fate (downwind of cloud edge) or organics (upwind) as the dominant non-refractory com-
 296 ponent; nitrate and ammonium account for higher mass fractions in the MBL than in
 297 the FT.

298 We acknowledge that assuming spatiotemporal homogeneity perpendicular to the
 299 mean wind is required for our quasi-Lagrangian analysis, whereas MBL and FT prop-
 300 erties vary upwind and across the wind. Even when a flight track aligns with MBL flow,
 301 the aircraft (speed \sim 100 m s $^{-1}$) is much faster than MBL horizontal winds (\sim 25 m s $^{-1}$).
 302 An example of spatial heterogeneity is evident on 8 March 2020 (Figure S8), where flight
 303 tracks are nearly perpendicular to the mean MBL wind. Samples farther offshore trav-
 304 eled longer periods over the ocean prior to cloud formation, and our analysis of both flights
 305 on that date indicate the FT acting briefly as a CCN source (Figure 3), which may be
 306 attributable to spatiotemporal variability neglected in our approach. Nonetheless, we ex-
 307 pect that the quasi-Lagrangian transformation is sufficient to reveal an overall pattern
 308 of FT dilution of MBL CCN, per Figures 2 and 3.

309 The MBL CCN budget analysis is subject to some additional potential weaknesses.
 310 First, we use CCN at a fixed SS = 0.43%, whereas collisional loss applies to aerosol par-
 311 ticles activated over a range of supersaturations. Second, the ERA5 reanalysis often over-
 312 estimates zonal winds in the region but values are expected to be within 10% (Belmonte Ri-
 313 vas & Stoffelen, 2019; Seethala et al., 2021). Third, we neglect chemical sources of CCN
 314 at any given SS, such as new particle formation (although MBL total aerosol surface ar-
 315 eas are unfavorable) and aqueous-phase processes that allow dissolved aerosol particles
 316 to activate at lower SS in subsequent cloud cycles (e.g., Y. Wang et al., 2021). Fourth,
 317 a chain of assumptions is required to construct MBL cloud profiles for collision-coalescence
 318 calculations. The sizable error bars in Figure 4 are intended to include these uncertain-
 319 ties.

320 Finally, we note that previous CAO observations (Abel et al., 2017) and simula-
 321 tions (Tornow et al., 2021) indicate even more rapid CCN loss during formation of in-
 322 tense precipitation. Based on inspection of cloud-regime transitions in satellite images
 323 compared with 2020 ACTIVATE CAO flight tracks, intense precipitation systematically
 324 occurs farther downwind than the observations analyzed here and could lead to rever-
 325 sal of the sign of the MBL–FT difference. CCN dilution from FT entrainment should
 326 accelerate this precipitation formation and subsequent transition towards open-cellular
 327 clouds.

328 The MBL aerosol entrainment documented here over the northwest Atlantic should
 329 widely occur in CAOs subject to FT dry intrusions (e.g., Jaeglé et al., 2017; Raveh-Rubin,
 330 2017), which bring descending air from higher altitudes with relatively low CCN con-
 331 centrations. CCN dilution is expected where the MBL is polluted, downwind of conti-
 332 nental CCN source regions. Earth system model results may be sensitive to precipita-

333 tion formation in such CAOs (D. T. McCoy et al., 2020), indicating a need to capture
 334 such aerosol dynamics in order to faithfully simulate cloud regime transitions.

335 5 Conclusions

336 A quasi-Lagrangian analysis of recent measurements collected during the ACTI-
 337 VATE field campaign is developed that supports the following conclusions:

- 338 - Cloud condensation nucleus (CCN) concentrations in the marine boundary layer
 339 (MBL) at supersaturations of 0.3 to 0.6%, as well as condensation nuclei larger
 340 than 10 nm, are predominantly far greater than in the free troposphere (FT) dur-
 341 ing cold-air outbreaks (CAOs) over the northwest Atlantic.
- 342 - Based on the research flight that reached farthest downwind, a budget analysis
 343 of CCN concentration in the MBL computed from available in-situ and remote-
 344 sensing measurements identifies MBL dilution from rapid entrainment of FT air
 345 as the primary sink of CCN upwind of cloud-regime transitions.
- 346 - CCN dilution from FT entrainment should accelerate precipitation formation and
 347 cloud closed-to-open cell transitions, reducing regional albedo in CAOs fed by sim-
 348 ilar FT air masses that are often associated with dry intrusions.

349 Open Research

350 All data is available at <https://www-air.larc.nasa.gov/cgi-bin/ArcView/activate>
 351 .2019. The R code written to evaluate data is available upon request.

352 Acknowledgments

353 This work was supported by ACTIVATE, a NASA Earth Venture Suborbital-3 (EVS-
 354 3) investigation funded by NASA's Earth Science Division and managed through the Earth
 355 System Science Pathfinder Program Office Division (grant no. 80NSSC19K044). We thank
 356 the ACTIVATE team for helpful discussion and for support with measurements and qual-
 357 ity control. Support by the German Science Foundation DFG within the SPP HALO
 358 1294 under grants VO1504/5-1, VO1504/7-1, and of the CRC TRR 301/1 TP Change
 359 is acknowledged.

360 References

- 361 Abel, S. J., Boulte, I. A., Waite, K., Fox, S., Brown, P. R. A., Cotton, R., ...
 362 Bower, K. N. (2017). The role of precipitation in controlling the transi-
 363 tion from stratocumulus to cumulus clouds in a northern hemisphere cold-air
 364 outbreak. *Journal of the Atmospheric Sciences*, 74(7), 2293 - 2314. Retrieved from <https://journals.ametsoc.org/view/journals/atsc/74/7/jas-d-16-0362.1.xml> doi: 10.1175/JAS-D-16-0362.1
- 365 Ackerman, A. S., Kirkpatrick, M., & Stevens, D. (2004). The impact of humidity
 366 above stratiform clouds on indirect aerosol climate forcing. *Nature*, 432, 1014–
 367 1017. Retrieved from <https://www.nature.com/articles/nature03174> doi:
 368 10.1038/nature03174
- 369 Albrecht, B. A. (1989). Aerosols, cloud microphysics, and fractional cloudiness. *Sci-
 370 ence*, 245(4923), 1227-1230. Retrieved from <https://www.science.org/doi/10.1126/science.245.4923.1227> doi: 10.1126/science.245.4923.1227
- 371 Atkinson, B. W., & Wu Zhang, J. (1996). Mesoscale shallow convection in
 372 the atmosphere. *Reviews of Geophysics*, 34(4), 403-431. Retrieved from
 373 <https://agupubs.onlinelibrary.wiley.com/doi/abs/10.1029/96RG02623>
 374 doi: <https://doi.org/10.1029/96RG02623>

- 378 Belmonte Rivas, M., & Stoffelen, A. (2019). Characterizing era-interim and era5
 379 surface wind biases using ascat. *Ocean Science*, 15(3), 831–852. Retrieved
 380 from <https://os.copernicus.org/articles/15/831/2019/> doi: 10.5194/os
 381 -15-831-2019
- 382 Bodas-Salcedo, A., Hill, P. G., Furtado, K., Williams, K. D., Field, P. R., Man-
 383 ners, J. C., ... Kato, S. (2016). Large contribution of supercooled liquid
 384 clouds to the solar radiation budget of the southern ocean. *Journal of Cli-
 385 mate*, 29(11), 4213 - 4228. Retrieved from [view/journals/climate/29/11/jcli-d-15-0564.1.xml](https://journals.ametsoc.org/

 386 <a href=) doi: 10.1175/
 387 JCLI-D-15-0564.1
- 388 Bretherton, C. S., Blossey, P. N., & Uchida, J. (2007). Cloud droplet sedimenta-
 389 tion, entrainment efficiency, and subtropical stratocumulus albedo. *Geophys-
 390 ical Research Letters*, 34(3). Retrieved from [wiley.com/doi/abs/10.1029/2006GL027648](https://agupubs.onlinelibrary.

 391 <a href=) doi: <https://doi.org/10.1029/2006GL027648>
- 392 Brümmer, B. (1999). Roll and cell convection in wintertime arctic cold-air out-
 393 breaks. *Journal of the Atmospheric Sciences*, 56(15), 2613 - 2636. Re-
 394 trievalved from https://journals.ametsoc.org/view/journals/atsc/56/15/1520-0469_1999_056_2613_racciw.2.0.co.2.xml doi: 10.1175/
 395 1520-0469(1999)056<2613:RACCIW>2.0.CO;2
- 396 Böhm, J. P. (1992). A general hydrodynamic theory for mixed-phase microphysics.
 397 part i: drag and fall speed of hydrometeors. *Atmospheric Research*, 27(4), 253-
 398 274. Retrieved from <https://www.sciencedirect.com/science/article/pii/0169809592900359> doi: [https://doi.org/10.1016/0169-8095\(92\)90035-9](https://doi.org/10.1016/0169-8095(92)90035-9)
- 400 Clarke, A. D., Owens, S. R., & Zhou, J. (2006). An ultrafine sea-salt flux from
 401 breaking waves: Implications for cloud condensation nuclei in the remote ma-
 402 rine atmosphere. *Journal of Geophysical Research: Atmospheres*, 111(D6).
 403 Retrieved from <https://agupubs.onlinelibrary.wiley.com/doi/abs/10.1029/2005JD006565> doi: 10.1029/2005JD006565
- 404 Dadashazar, H., Braun, R. A., Crosbie, E., Chuang, P. Y., Woods, R. K., Jon-
 405 sson, H. H., & Sorooshian, A. (2018). Aerosol characteristics in the en-
 406 trainment interface layer in relation to the marine boundary layer and free
 407 troposphere. *Atmospheric Chemistry and Physics*, 18(3), 1495-1506. Re-
 408 trievalved from <https://acp.copernicus.org/articles/18/1495/2018/> doi:
 409 10.5194/acp-18-1495-2018
- 410 Dadashazar, H., Painemal, D., Alipanah, M., Brunke, M., Chellappan, S., Corral,
 411 A. F., ... Sorooshian, A. (2021). Cloud drop number concentrations over the
 412 western north atlantic ocean: seasonal cycle, aerosol interrelationships, and
 413 other influential factors. *Atmospheric Chemistry and Physics*, 21(13), 10499-
 414 10526. Retrieved from <https://acp.copernicus.org/articles/21/10499/2021/> doi: 10.5194/acp-21-10499-2021
- 415 Etling, D., & Brown, R. A. (1993). Roll vortices in the planetary boundary
 416 layer: A review. *Boundary-Layer Meteorology*, 65(3), 215-248. Retrieved
 417 from <https://link.springer.com/article/10.1007/BF00705527> doi:
 418 10.1007/BF00705527
- 419 Field, P. R., Brozkova, R., Chen, M., Dudhia, J., Lac, C., Hara, T., ... McTaggart-
 420 Cowan, R. (2017). Exploring the convective grey zone with regional
 421 simulations of a cold air outbreak. *Quarterly Journal of the Royal Me-
 422 teorological Society*, 143(707), 2537-2555. Retrieved from <https://rmets.onlinelibrary.wiley.com/doi/full/10.1002/qj.3105> doi:
 423 <https://doi.org/10.1002/qj.3105>
- 424 Field, P. R., & Wood, R. (2007). Precipitation and cloud structure in midlatitude
 425 cyclones. *Journal of Climate*, 20(2), 233 - 254. Retrieved from <https://journals.ametsoc.org/view/journals/clim/20/2/jcli3998.1.xml> doi: 10
 426 .1175/JCLI3998.1

- 433 Forbes, R. M., & Ahlgrimm, M. (2014). On the representation of high-latitude
 434 boundary layer mixed-phase cloud in the ecmwf global model. *Monthly*
 435 *Weather Review*, 142(9), 3425 - 3445. Retrieved from <https://journals.ametsoc.org/view/journals/mwre/142/9/mwr-d-13-00325.1.xml> doi:
 436 10.1175/MWR-D-13-00325.1
- 437 Fridlind, A. M., Ackerman, A. S., Chaboureau, J.-P., Fan, J., Grabowski, W. W.,
 438 Hill, A. A., ... Zhang, M. (2012). A comparison of twp-ice observational data
 439 with cloud-resolving model results. *Journal of Geophysical Research: Atmo-*
 440 *spheres*, 117(D5). Retrieved from <https://agupubs.onlinelibrary.wiley.com/doi/abs/10.1029/2011JD016595> doi: 10.1029/2011JD016595
- 441 Hall, W. D. (1980). A detailed microphysical model within a two-dimensional
 442 dynamic framework: Model description and preliminary results. *Journal*
 443 *of Atmospheric Sciences*, 37(11), 2486 - 2507. Retrieved from https://journals.ametsoc.org/view/journals/atsc/37/11/1520-0469_1980_037_2486_admmwa_2.0_co_2.xml doi: 10.1175/1520-0469(1980)037(2486:
 444 ADMMWA)2.0.CO;2
- 445 Jaeglé, L., Wood, R., & Wargan, K. (2017). Multiyear composite view of ozone
 446 enhancements and stratosphere-to-troposphere transport in dry intrusions
 447 of northern hemisphere extratropical cyclones. *Journal of Geophysical Re-*
 448 *search: Atmospheres*, 122(24), 13,436-13,457. Retrieved from <https://agupubs.onlinelibrary.wiley.com/doi/abs/10.1002/2017JD027656> doi:
 449 <https://doi.org/10.1002/2017JD027656>
- 450 Lance, S., Nenes, A., Medina, J., & Smith, J. N. (2006). Mapping the operation of
 451 the dmt continuous flow ccn counter. *Aerosol Science and Technology*, 40(4),
 452 242-254. Retrieved from <https://doi.org/10.1080/02786820500543290> doi:
 453 10.1080/02786820500543290
- 454 Lawson, R. P., O'Connor, D., Zmarzly, P., Weaver, K., Baker, B., Mo, Q., & Jon-
 455 sson, H. (2006). The 2d-s (stereo) probe: Design and preliminary tests of
 456 a new airborne, high-speed, high-resolution particle imaging probe. *Jour-*
 457 *nal of Atmospheric and Oceanic Technology*, 23(11), 1462 - 1477. Re-
 458 tried from https://journals.ametsoc.org/view/journals/atot/23/11/jtech1927_1.xml doi: 10.1175/JTECH1927.1
- 459 Li, X.-Y., Wang, H., Chen, J., Endo, S., George, G., Cairns, B., ... Zuidema, P.
 460 (2021). Large-eddy simulations of marine boundary-layer clouds associated
 461 with cold air outbreaks during the activate campaign– part 1: Case setup and
 462 sensitivities to large-scale forcings. *Journal of the Atmospheric Sciences*. Re-
 463 tried from <https://journals.ametsoc.org/view/journals/atsc/aop/JAS-D-21-0123.1.xml> doi: 10.1175/JAS-D-21-0123.1
- 464 Lilly, D. K. (1968). Models of cloud-topped mixed layers under a strong inversion.
 465 *Quarterly Journal of the Royal Meteorological Society*, 94(401), 292-309. Re-
 466 tried from <https://rmets.onlinelibrary.wiley.com/doi/abs/10.1002/qj.49709440106> doi: <https://doi.org/10.1002/qj.49709440106>
- 467 McCoy, D. T., Field, P., Bodas-Salcedo, A., Elsaesser, G. S., & Zelinka, M. D.
 468 (2020). A regime-oriented approach to observationally constraining extrat-
 469 ropical shortwave cloud feedbacks. *Journal of Climate*, 33(23), 9967 - 9983.
 470 Retrieved from <https://journals.ametsoc.org/view/journals/clim/33/23/jcliD190987.xml> doi: 10.1175/JCLI-D-19-0987.1
- 471 McCoy, I. L., Bretherton, C. S., Wood, R., Twohy, C. H., Gettelman, A., Bardeen,
 472 C. G., & Toohey, D. W. (2021). Influences of recent particle formation
 473 on southern ocean aerosol variability and low cloud properties. *Journal of*
 474 *Geophysical Research: Atmospheres*, 126(8), e2020JD033529. Retrieved
 475 from <https://agupubs.onlinelibrary.wiley.com/doi/abs/10.1029/2020JD033529> doi: <https://doi.org/10.1029/2020JD033529>
- 476 Moore, R. H., & Nenes, A. (2009). Scanning flow ccn analysis—a method for fast
 477 measurements of ccn spectra. *Aerosol Science and Technology*, 43(12), 1192-
 478

- 488 1207. Retrieved from <https://doi.org/10.1080/02786820903289780> doi: 10
 489 .1080/02786820903289780
- 490 Painemal, D., Corral, A. F., Sorooshian, A., Brunke, M. A., Chellappan, S.,
 491 Afzali Gorooh, V., ... Zuidema, P. (2021). An overview of atmospheric
 492 features over the western north atlantic ocean and north american east
 493 coast—part 2: Circulation, boundary layer, and clouds. *Journal of Geophysical
 494 Research: Atmospheres*, 126(6), e2020JD033423. Retrieved from <https://agupubs.onlinelibrary.wiley.com/doi/abs/10.1029/2020JD033423> doi:
 495 <https://doi.org/10.1029/2020JD033423>
- 496 Papritz, L., Pfahl, S., Sodemann, H., & Wernli, H. (2015). A climatology of cold
 497 air outbreaks and their impact on air–sea heat fluxes in the high-latitude
 498 south pacific. *Journal of Climate*, 28(1), 342 - 364. Retrieved from <https://journals.ametsoc.org/view/journals/clim/28/1/jcli-d-14-00482.1.xml>
 499 doi: 10.1175/JCLI-D-14-00482.1
- 500 Papritz, L., & Spengler, T. (2017). A lagrangian climatology of wintertime cold
 501 air outbreaks in the irminger and nordic seas and their role in shaping air–sea
 502 heat fluxes. *Journal of Climate*, 30(8), 2717 - 2737. Retrieved from <https://journals.ametsoc.org/view/journals/clim/30/8/jcli-d-16-0605.1.xml>
 503 doi: 10.1175/JCLI-D-16-0605.1
- 504 Pincus, R., & Baker, M. B. (1994). Effect of precipitation on the albedo suscep-
 505 tibility of clouds in the marine boundary layer. *Nature*, 372(6503), 250 - 252.
 506 Retrieved from <https://www.nature.com/articles/372250a0> doi: 10.1038/
 507 372250a0
- 508 Pithan, F., Svensson, G., Caballero, R., Chechin, D., Cronin, T. W., Ekman,
 509 A. M. L., ... Wendisch, M. (2019). Role of air-mass transformations in
 510 exchange between the arctic and mid-latitudes. *Nature Geoscience*, 11, 805-
 511 812. Retrieved from <https://www.nature.com/articles/s41561-018-0234-1>
 512 doi: 10.1038/s41561-018-0234-1
- 513 Raveh-Rubin, S. (2017). Dry intrusions: Lagrangian climatology and dynamical
 514 impact on the planetary boundary layer. *Journal of Climate*, 30(17), 6661 -
 515 6682. Retrieved from <https://journals.ametsoc.org/view/journals/clim/30/17/jcli-d-16-0782.1.xml> doi: 10.1175/JCLI-D-16-0782.1
- 516 Roberts, G. C., & Nenes, A. (2005). A continuous-flow streamwise thermal-gradient
 517 ccn chamber for atmospheric measurements. *Aerosol Science and Technology*,
 518 39(3), 206-221. Retrieved from <https://doi.org/10.1080/027868290913988>
 519 doi: 10.1080/027868290913988
- 520 Rémillard, J., & Tselioudis, G. (2015). Cloud regime variability over the azores and
 521 its application to climate model evaluation. *Journal of Climate*, 28(24), 9707 -
 522 9720. Retrieved from <https://journals.ametsoc.org/view/journals/clim/28/24/jcli-d-15-0066.1.xml> doi: 10.1175/JCLI-D-15-0066.1
- 523 Seethala, C., Zuidema, P., Edson, J., Brunke, M., Chen, G., Li, X.-Y., ... Ziembra,
 524 L. (2021). On assessing era5 and merra2 representations of cold-air outbreaks
 525 across the gulf stream. *Geophysical Research Letters*, 48(19), e2021GL094364.
 526 Retrieved from <https://agupubs.onlinelibrary.wiley.com/doi/abs/10.1029/2021GL094364> doi: <https://doi.org/10.1029/2021GL094364>
- 527 Sorooshian, A., Anderson, B., Bauer, S. E., Braun, R. A., Cairns, B., Crosbie,
 528 E., ... Zuidema, P. (2019). Aerosol–cloud–meteorology interaction air-
 529 borne field investigations: Using lessons learned from the u.s. west coast
 530 in the design of activate off the u.s. east coast. *Bulletin of the Ameri-
 531 can Meteorological Society*, 100(8), 1511 – 1528. Retrieved from <https://journals.ametsoc.org/view/journals/bams/100/8/bams-d-18-0100.1.xml>
 532 doi: 10.1175/BAMS-D-18-0100.1
- 533 Tornow, F., Ackerman, A. S., & Fridlind, A. M. (2021). Preconditioning of
 534 overcast-to-broken cloud transitions by riming in marine cold air outbreaks.
 535 [Atmospheric Chemistry and Physics](https://doi.org/10.1029/2020AC014207), 21(15), 12049–12067. Retrieved
 536 from <https://doi.org/10.1029/2020AC014207>

- 543 from <https://acp.copernicus.org/articles/21/12049/2021/> doi:
544 10.5194/acp-21-12049-2021
- 545 Tselioudis, G., Rossow, W. B., Jakob, C., Remillard, J., Tropf, D., & Zhang, Y.
546 (2021). Evaluation of clouds, radiation, and precipitation in cmip6 models
547 using global weather states derived from isccp-h cloud property data. *Journal
548 of Climate*, 34(17), 7311 - 7324. Retrieved from <https://journals.ametsoc.org/view/journals/clim/aop/JCLI-D-21-0076.1/JCLI-D-21-0076.1.xml>
549 doi: 10.1175/JCLI-D-21-0076.1
- 550 Twomey, S. (1974). Pollution and the planetary albedo. *Atmospheric Environment*
551 (1967), 8(12), 1251-1256. Retrieved from <https://www.sciencedirect.com/science/article/pii/0004698174900043> doi: [https://doi.org/10.1016/0004-6981\(74\)90004-3](https://doi.org/10.1016/0004-6981(74)90004-3)
- 551 Wang, H., & Feingold, G. (2009). Modeling mesoscale cellular structures and drizzle
552 in marine stratocumulus. part i: Impact of drizzle on the formation and evolution
553 of open cells. *Journal of the Atmospheric Sciences*, 66(11), 3237 - 3256.
554 Retrieved from <https://journals.ametsoc.org/view/journals/atsc/66/11/2009jas3022.1.xml> doi: 10.1175/2009JAS3022.1
- 555 Wang, Y., Zheng, G., Jensen, M. P., Knopf, D. A., Laskin, A., Matthews, A. A.,
556 ... Wang, J. (2021). Vertical profiles of trace gas and aerosol properties
557 over the eastern north atlantic: variations with season and synoptic condition.
558 *Atmospheric Chemistry and Physics*, 21(14), 11079–11098. Retrieved
559 from <https://acp.copernicus.org/articles/21/11079/2021/> doi:
560 10.5194/acp-21-11079-2021
- 561 Wood, R. (2006). Rate of loss of cloud droplets by coalescence in warm clouds.
562 *Journal of Geophysical Research: Atmospheres*, 111(D21). Retrieved
563 from <https://agupubs.onlinelibrary.wiley.com/doi/abs/10.1029/2006JD007553> doi: <https://doi.org/10.1029/2006JD007553>
- 564 Wood, R., Stemmler, J. D., Rémillard, J., & Jefferson, A. (2017). Low-ccn concen-
565 tration air masses over the eastern north atlantic: Seasonality, meteorology,
566 and drivers. *Journal of Geophysical Research: Atmospheres*, 122(2), 1203-
567 1223. Retrieved from <https://agupubs.onlinelibrary.wiley.com/doi/abs/10.1002/2016JD025557> doi: 10.1002/2016JD025557
- 568 Yamaguchi, T., Feingold, G., & Kazil, J. (2017). Stratocumulus to cumulus transi-
569 tion by drizzle. *Journal of Advances in Modeling Earth Systems*, 9(6),
570 2333-2349. Retrieved from <https://agupubs.onlinelibrary.wiley.com/doi/full/10.1002/2017MS001104> doi: 10.1002/2017MS001104
- 571 Zheng, G., Sedlacek, A. J., Aiken, A. C., Feng, Y., Watson, T. B., Raveh-Rubin,
572 S., ... Wang, J. (2020). Long-range transported north american wild-
573 fire aerosols observed in marine boundary layer of eastern north atlantic.
574 *Environment International*, 139, 105680. Retrieved from <https://www.sciencedirect.com/science/article/pii/S0160412019326480> doi:
575 <https://doi.org/10.1016/j.envint.2020.105680>
- 576 Zheng, G., Wang, Y., Wood, R., Jensen, M. P., Kuang, C., McCoy, I. L., ... Wang,
577 J. (2021). New particle formation in the remote marine boundary layer. *Nature
578 Communications*, 12(1), 527. Retrieved from <https://www.nature.com/articles/s41467-020-20773-1> doi: 10.1038/s41467-020-20773-1
- 578